# Degree of polarization of luminescence from InP under SiN stripes: fits to FEM simulations

Daniel T Cassidy, Jean-Pierre Landesman

## To cite this version:

Daniel T Cassidy, Jean-Pierre Landesman. Degree of polarization of luminescence from InP under SiN stripes: fits to FEM simulations. Optics Continuum , 2023, 2 (6), pp.1505-1522. 10.1364/optcon.481902 . hal-04133163

HAL Id: hal-04133163
https://hal.science/hal-04133163

Submitted on 19 Jun 2023

Research Article Vol. 2, No. 6 / 15 Jun 2023 / *Optics Continuum* 1505

OPTICS CONTINUUM

# Degree of polarization of luminescence from InP under SiN stripes: fits to FEM simulations

**DANIEL T. CASSIDY[1,*] AND AND JEAN-PIERRE LANDESMAN[2,3]**

[1] *McMaster University, Department of Engineering Physics, Hamilton, ON L8S 4L7, Canada*
[2] *Université de Rennes, INSA Rennes, CNRS, Institut FOTON–UMR 6082, 35000 Rennes, France*
[3] *jean-pierre.landesman@univ-rennes1.fr*
[*] *cassidy@mcmaster.ca*

**Abstract:** Fits of 3D finite element method (FEM) simulations to the degree of polarization (DOP) of photoluminescence (PL) measured on facets under SiN stripes on InP substrates are presented. The measured data is low noise and the fits are remarkably good; lobes owing to defects (perhaps dislocations) can be seen in false colour maps of the residues from the least squares fits. It is found that the vast majority (estimated to be $> 99\%$) of the DOP patterns can be attributed to an initial condition for the FEM simulations of biaxial strain in the SiN stripes. In addition to the fits of FEM simulations to the data and discussion of the fits: fits of error functions to PL data to find the resolution of the optical system and the location of the top surface, quantities that are required in fits of 3D FEM simulations to the data, are presented; as is presented some historical information on analysis of luminescent III-V materials and devices by analysis of the DOP of the luminescence, and some information on the dependence of the DOP of luminescence on strain for InP.

## 1. Introduction

Semiconductor diode lasers and photonics integrated circuits, like Si integrated circuits, are composed of multiple layers of different materials and are subjected to different temperatures in the processes of fabrication. These multiple materials have different material properties, including different lattice constants and coefficients of thermal expansion, which lead to non-uniform and possibly localised mechanical strain in the materials.

Mechanical strain in a semiconductor diode laser or a photonics integrated circuit (PIC) can affect the operation of the laser or PIC through changes to the refractive indices or through movement of defects.

The effect of strain on an optical device is easy to demonstrate. Figures 2 and 3 of Ref. [1] show the near-field output of a waveguide changing from multimode to single mode upon removal of the metal and dielectric layers over the ridge waveguide. The waveguide of Ref. [1] is a simple 'toy model' as compared to modern PICs, yet operation of the simple toy model was impacted by strain.

DFB lasers are more complicated than a waveguide. Morrison *et al.* [2] showed that minute changes in the orientation of the bonding tool resulted in measurable changes in the strain profile and in the operation of DFB lasers that were bonded active region up.

The effect of strain on the operational lifetime of devices is perhaps more difficult to show than the effect of stress on the wave guiding properties as life testing is time consuming and statistical in nature. Nevertheless, strain as introduced by bonding devices to different substrates using different methods of attachments showed differences in estimated lifetimes of GaAs-based lasers [3]. One explanation for the strain-dependent lifetime of devices is that non-uniform strain is a motive force that moves pre-existing defects to the active region where the defects condense and affect operation of the device [4].

#481902 https://doi.org/10.1364/OPTCON.481902
Journal © 2023 Received 23 Nov 2022; revised 11 May 2023; accepted 23 May 2023; published 15 Jun 2023

To understand and to optimize operation of semiconductor lasers and PICs, it is helpful to have a method to measure strain in the devices. One method to estimate strain in luminescent III-V materials and devices is by measurement and analysis of the degree of polarization (DOP) of the luminescence. This paper is about characterizing strain from SiN stripes on InP through DOP measurements and finite element method (FEM) simulations.

### 1.1. Organization of this paper

Background information, results, discussion of the results, and a conclusion are presented in the next sections. The Appendix provides information on the degeneracy of the facet strain fields under a biaxially strained SiN stripe on InP and hence on the ability to use the measured DOP to distinguish between an isotropic model ($DOP$) and and a non-isotropic model ($DOP_{110}$).

## 2. Background

The degree of polarization (DOP) and rotated degree of polarization (ROP) of luminescence from direct band gap III-V materials and devices are sensitive functions of strain in the materials and devices [5–8]. The DOP was defined to be

$$DOP = \frac{L_h - L_v}{L_h + L_v} \tag{1}$$

where $L_h$ and $L_v$ are the measured linearly polarized luminescences in two orthogonal directions, $h$ and $v$, for light that is emitted normal to the measurement surface [5]. In general, the measured DOP depends on the choice of alignment of the measurement coordinate system relative to the crystal directions of the III-V sample.

The form of Eq. (1) was chosen from familiarity of the definition of fringe visibility: $V = (I_{\max} - I_{\min})/(I_{\max} + I_{\min})$, where $I_{\max}$ and $I_{\min}$ are the maximum and minimum intensities in an interference experiment [9, pg 267], with $I_{\max}$ replaced by $L_h$ and $I_{\min}$ replaced by $L_v$. Fringe visibility ranges from 0 to 1 and is independent of the strengths of the interfering beams.

The DOP, as defined, ranges from $-1$ to $+1$ and is independent of the measured total luminescence, $L_h + L_v$. The horizontal direction was chosen to replace $I_{\max}$ because measurements were being made of the DOP of electroluminescence from III-V semiconductor diode lasers [5]. These lasers were mounted horizontally and the TE mode, which was polarized along the horizontal direction, was the most likely mode to lase. TE dominant operation was indicated by $DOP>0$. Occasionally lasers would operate with more TM polarized light than TE polarized light, which would give a $DOP<0$. Any measure of the DOP of luminescence that gave only the magnitude of the DOP would not differentiate between TE and TM operation.

The ROP was later defined to be [10–12]

$$ROP = \frac{L_{h'} - L_{v'}}{L_{h'} + L_{v'}} \tag{2}$$

where $h'$ and $v'$ are two orthogonal directions that are obtained by rotation of the $h$-$v$ coordinate system by a $-45$ deg rotation about the exterior normal to the measurement surface. This second measurement of the DOP of the luminescence is independent of the measurement defined by Eq. (1) and provides additional information on the strain in the sample.

The predicted dependences of DOP and ROP on strain, for isotropic material [13, Sec. 4.A.1] and for $\{001\}$ GaAs or InP surfaces, with $h$ and $v$ along $\langle 100\rangle$ and $\langle 010\rangle$ directions and $h'$ and $v'$

along $\langle 110\rangle$ and $\langle 1\bar{1}0\rangle$ directions [13, Secs. 3.D.1 and 3.D.3], are given by

$$DOP = -|K_e|\,(e_1 - e_2) \tag{3}$$

and

$$ROP = |K_e|\,(2\,e_6) \tag{4}$$

where $e_1$ is the strain along the $h$ direction, $e_2$ is the strain along the $v$ direction, and $e_6 = e_{12}$ is the tensor shear strain, with the calibration constant $K_e = -3\,b/(4\,k_B T)$ [13, Eq. (26)], [14, Eq. (16)]. The calibration constant $K_e$ is a function of the shear deformation potential $b$, the Boltzmann constant $k_B = 8.6173 \times 10^{-5}$ eV K$^{-1}$, and the temperature $T$. With $b = -2$ eV [15] and $T = 296 \pm 3$ K, $K_e = 58.8 \mp 0.6$. Note that we use $h$ and $v$ as two orthogonal directions in the plane of the surface that is being measured. Usually the sample is aligned so that $h$ or $v$ point along a crystal axis.

Experimentally, the calibration constant for InP was estimated to be 65 ± 10 [16, pp 101–103], as estimated by fits of the measured DOP and the measured ROP from v-grooves under bending moments to the predicted DOP and ROP from Eqs. (3) and (4) with the strain fields obtained from 2D FEM simulations [8]. For GaAs, the calibration constant was estimated experimentally to be 50 ± 10 [16] based on bars placed under bending moments [7,10].

If the two orthogonal measurement axes are not along equivalent crystal directions, such as for measurement from a $\{110\}$ facet plane with $h$ along a $\langle 1\bar{1}0\rangle$ direction and $v$ along an inequivalent $\langle 001\rangle$ direction, expressions for the dependence of DOP and ROP on strain are not as simple as for the two orthogonal measurements axes along equivalent crystal directions.

For an InP facet and assuming $d = 2.5\,b$ [15, Table VI, pg 5829], the predicted relationships [13, Sec. 3.D.4], [14, Sec. 2.E] are,

$$DOP_{110} = -|K_e|\,(1.315\,e_1 - 0.7987\,e_3) \tag{5}$$

and

$$ROP_{110} = |K_e|\,1.463\,(2\,e_5), \tag{6}$$

with the calibration constant $K_e = -3\,b/(4\,k_B T)$ [13, Eq. (26)], [14, Eq. (16)], and where the normal to the facet is a $\langle 110\rangle$ direction, $h$ and $e_1$ are in the plane of the facet and along a $\langle 1\bar{1}0\rangle$ direction, and $v$ and $e_3$ are in the growth or $\langle 001\rangle$ direction. We consider this alignment of sample and measurement coordinate systems to be the usual alignment. Figures showing this usual alignment of coordinate systems are in Refs. [8,14].

Note that the DOP and ROP variables in Eqs. (5) and (6) are subscripted with the normal to the measurement surface. In principal, one should subscript the variables with the unevaluated expression $\hat{\boldsymbol{h}} \times \hat{\boldsymbol{v}}$ where $\hat{\boldsymbol{h}}$ and $\hat{\boldsymbol{v}}$ are unit vectors that point along the $h$ and $v$ directions. This notation is cumbersome, i.e., $DOP_{\langle 1\bar{1}0\rangle \times \langle 001\rangle}$ is precise but cumbersome to write, and we rely on the understanding that the usual alignment of sample and measurement coordinate systems is employed for the surface given by the subscript on the DOP and ROP variables.

In addition, as necessary the adjective ‘measured’ will be used to distinguish between the use of Eqs. (1) and (2) to evaluate the DOP or ROP and the use of Eqs. (3) – (6) to evaluate the same variable. Thus measured $DOP_{110}$ means the DOP determined by measurement and manipulation of $L_h$ and $L_v$ as indicated in Eq. (1), with $h$ and $v$ the two usual orthogonal directions in a $\{110\}$ plane. Similar interpretations apply for measured $DOP$, measured $ROP$, and measured $ROP_{110}$. Again, the subscripts on DOP and ROP give the normal to the measurement surface, and the horizontal and vertical directions follow the ‘usual’ alignment of coordinate systems.

The expressions for the dependence of DOP and ROP on strain are based on Bahder’s analytic expressions for the strain-dependent dispersions using an eight band $\boldsymbol{k} \cdot \boldsymbol{p}$ model for strained III-V materials [17–19]. As explained in [13], strain leads to $\boldsymbol{k}$-dependent distortions in the energy bands, and since for parabolic bands the direction of polarization of emission lies along the direction of $\boldsymbol{k}$, the $\boldsymbol{k}$-dependent distortions give rise to a strain-dependent degree of polarization subject to the condition that any emission must be a transversely polarized wave.

Figure 1 plots $E(\theta)$ for $\pi \leq \theta \leq \pi$, with $k_x = k_y = 0.03\ \cos(\theta)/\sqrt{2}$ and $k_z = 0.03\ \sin(\theta)$, in units where $\hbar/\sqrt{m_o} = 1$; with $e_3 = 0.001$; and, with all other strains equal to zero, where $k_x$, $k_y$, and $k_z$ are the components of the crystal momentum $\boldsymbol{k} = (k_x, k_y, k_z)$ in the crystal coordinate system. The angle $\theta$ specifies a direction in space: $\theta = 0$ is along the horizontal direction and $\theta = \pi/2$ is along a vertical direction. The energy $E(\theta)$ is calculated as the conduction band energy minus the valence band energy using Bahder's analytic expressions.

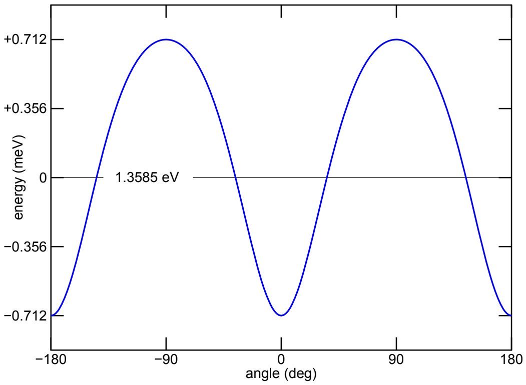

**Fig. 1.** Plot of $E(\theta)$ as a function of the angle $\theta$, for $k_x = k_y = 0.03\ \cos(\theta)/\sqrt{2}$, $k_z = 0.03\ \sin(\theta)$, $e_3 = 0.001$, and all other strains equal to zero.

Strain creates $\boldsymbol{k}$-dependent energy 'wells' in the dispersion. The dependence of the energy on strain and crystal momentum gives rise to a degree of polarization of luminescence that is strain dependent.

Figure 2 plots $E(\theta)^2\ \exp(-E(\theta)/k_BT)$ for the same parameters as chosen for Fig. 1. The magnitude of the crystal momentum was chosen to give an energy roughly $k_BT/2$ above the band edge, an energy where the carrier density should be a maximum for a parabolic band. The function $E(\theta)^2\ \exp(-E(\theta)/k_BT)$ mimics a density of optical states times an occupation probability for carriers and should crudely describe the relative rate of transitions at an energy $E(\theta)$ assuming the absorption coefficient $\alpha(E(\theta))$ is a non-zero constant above the band gap [20, Eq. (10)].

The measured $DOP_{110}$ for the usual alignment of crystal and measurement axes would detect the light polarized along $\theta = 0$, the $h$ direction, minus the light polarized along $\theta = \pi/2$, the $v$ direction. From Fig. 2, it is clear that the measured $DOP_{110}$ is non-zero. The strain has created $k$-dependent energy 'wells' in the band structure; these 'wells' will emit more light, with the light linearly polarized along the direction of the crystal momentum $\boldsymbol{k}$ of the carriers involved in the radiative transition.

The measured $ROP_{110}$ for the usual alignment of crystal and measurement axes would detect the light polarized along $\theta = -\pi/4$, the $h'$ direction, minus the light polarized along $\theta = \pi/4$, the $v'$ direction. From Fig. 2, it is clear that the measured $ROP_{110}$ is zero. There is no shear strain for the calculations used to create Figs. 1 and 2, and thus no measured $ROP_{110}$ for the relative rates of emission shown in Fig. 2.

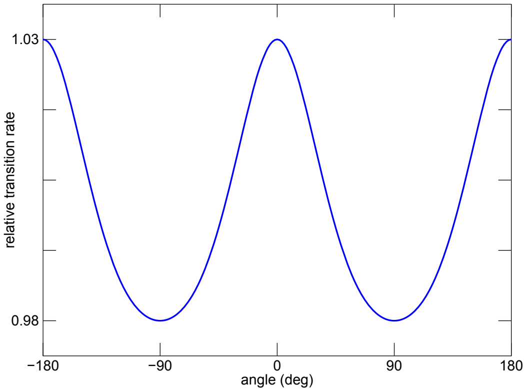

**Fig. 2.** Plot of $E(\theta)^2\,\exp\left(-E(\theta)/k_BT\right)$ as a function of the angle $\theta$, for $k_x = k_y = 0.03\,\cos(\theta)/\sqrt{2}$, $k_z = 0.03\,\sin(\theta)$, $e_3 = 0.001$, and all other strains equal to zero.

### 2.1. Least squares fits

Functions of the form

$$f_{DOP}(h_i, v_j) = \sum_{k=1}^{n} a_k\, g_k^{(DOP)}(h_i, v_j) + a_{n+1} + a_{n+2}\,(v_j - \bar{v}_j) + a_{n+3}\,(h_i - \bar{h}_i) + a_{n+4}\,(v_j - \bar{v}_j)^2 + a_{n+5}\,(h_i - \bar{h}_i)^2 + a_{n+6}\,\frac{(v_j - \bar{v}_j)\,(h_i - \bar{h}_i)}{100} \tag{7}$$

and

$$f_{ROP}(h_i, v_j) = \sum_{k=1}^{n} R_a\, a_k\, g_k^{(ROP)}(h_i, v_j) + b_1 + b_2\,(v_j - \bar{v}_j) + b_3\,(h_i - \bar{h}_i) + b_4\,(v_j - \bar{v}_j)^2 + b_5\,(h_i - \bar{h}_i)^2 + b_6\,\frac{(v_j - \bar{v}_j)\,(h_i - \bar{h}_i)}{100} \tag{8}$$

were fit to the measured $DOP_{110}$ and $ROP_{110}$ data using a linear least squares technique [21, Ch. 7]. In Eq. (7), the $a_k, k = 1..n + 6$, are the fit coefficients, $g_k^{(DOP)}(h_i, v_j)$ are $n$ basis functions from the FEM simulation interpolated on the same grid as the grid on which the data were measured, and $\bar{h}_i$ and $\bar{v}_j$ are the mean values for the horizontal points $h_i$ and the vertical points $v_j$.

The basis functions are solutions from the FEM simulations for a given initial condition, such as biaxial stress in the SiN stripe. The FEM simulation will find the stress and strain fields or basis function that satisfy the boundary conditions given an initial starting point. For brevity, we label the basis functions by the initial condition (such as a basis function of biaxial stress) and expect the reader to remember that a basis function is the FEM solution to the initial condition.

For Eq. (8), $R_a$ is a constant with respect to the fitting procedure. The decision to use the same fit parameter $a_k, k = 1..n$ for both the measured DOP and ROP data was motivated by the fact that for a given influence, the ratio of the magnitudes of the $g_k^{(DOP)}(h_i, v_j)$ and $g_k^{(ROP)}(h_i, v_j)$ basis functions should be unity. If the possibilities presented by either the pair of Eqs. (3) and (4) or the pair of Eqs. (5) and (6) are correct, then $R_a = 1$. The 'constant' $R_a$ was included as a means to check the accuracy of the expressions for the dependence of DOP and ROP on strain.

The ratio $R_a$ was determined by repeated fitting with different values for $R_a$ and choosing the value that produced a best fit.

Of the fit parameters, $a_{n+1}$ to $a_{n+6}$ and $b_1$ to $b_6$ account for background signals in the measured $DOP_{110}$ and $ROP_{110}$ data. These background signals are unavoidable artefacts of the measurement system such as birefringence in the optics, and include any unwanted patterns, many of which might be alignment dependent [22].

The $2\,n$ basis functions $g_k^{(DOP)}(h_i, v_j)$ and $g_k^{(ROP)}(h_i, v_j)$, $k = 1..n$ are initial conditions to the FEM simulations and allow for multiple influences on the sample. For example, biaxial stress in the SiN will cause one response, as will uniaxial stress in the SiN, as will damaged InP surfaces caused by processing steps such as etching and polishing. The response to each influence (which is an initial condition for the simulation) is calculated independently through a 3D FEM simulation, and using the fact that the FEM simulations employ linear elasticity, the principle of linear superposition is employed to find through a least squares algorithm the contribution of each influence to the measured DOP and ROP distributions. This approach also allows one to investigate the effects of different influences on the DOP and ROP distributions. We call the influences 'basis functions' based on the idea that the final distribution is synthesized by addition of properly weighted basis functions. The fit parameters provide the proper weighting of each basis function.

### *2.2. Reduced chi-square variate*

Least squares fitting involves finding the set of fit parameters $\{a_k\}$ and $\{b_k\}$ that minimize reduced chi-square, $\chi_T^2$, where

$$\chi_T^2 = \frac{\nu_a\ \chi_{DOP}^2 + \nu_b\ \chi_{ROP}^2}{\nu_a + \nu_b} \tag{9}$$

with

$$\chi_{DOP}^2 = \sum_{i=1}^{N_h} \sum_{j=1}^{N_v} \frac{\left(DOP(h_i, v_j) - f_{DOP}(h_i, v_j)\right)^2}{\nu_a\,\sigma^2(h_i, v_j)} \tag{10}$$

and

$$\chi_{ROP}^2 = \sum_{i=1}^{N_h} \sum_{j=1}^{N_v} \frac{\left(ROP(h_i, v_j) - f_{ROP}(h_i, v_j)\right)^2}{\nu_b\,\sigma^2(h_i, v_j)}. \tag{11}$$

$DOP(h_i, v_j)$ is the measured DOP at one of $N_h N_v$ locations $(h_i, v_j), i = 1..N_h, j = 1..N_v$, $f_{DOP}(h_i, v_j)$ is the simulated or estimated value at $(h_i, v_j)$, and $\sigma^2(h_i, v_j)$ is the variance for $DOP(h_i, v_j)$. $\nu_a$ is the number of degrees of freedom for the DOP data, which equals the total number of data points $N_h \times N_v$ minus the number of independent variables used to specify $f_{DOP}(h_i, v_j)$. Typically, $N_h = 101$ and $N_v \approx 85$, for a number of degrees of freedom $\nu_a$ of $\approx 8500$. The number of fit parameters is insignificant when compared to the number of data points.

The equations for the fit to the ROP data have a similar interpretation.

The least squares fitting found the simultaneous best fit to both the DOP and ROP data files. This should be a realistic approach as both the ROP and DOP are measured simultaneously from data acquired from the same point. It is possible to find minimum values for $\chi_{DOP}$ and for $\chi_{ROP}$ for different registrations of the measured data and the simulations.

The value of $\sigma^2(h_i, v_j)$ was estimated from the data by setting $\chi_T = 1$ for one of the fits and by assuming that the value of $\sigma^2(h_i, v_j)$ was the same for each data point and file type.

## 3. Results

The data were obtained with the set-up described in [8]. In this set-up a frequency stabilized mechanical optical chopper was used so that measurements of the total luminescence could be made in the varying light conditions and away from the $1/f$ noise that dominates at low frequencies. With use of a mechanical chopper, there is no need to place the measurement system in a light-tight box.

The luminescence for analysis of the degree of polarization was photoluminescence (PL). PL is generated near the surface of InP, so the strains of interest are those near the measurement surface from which the light is collected. The measurements were made on a cleaved surface, with the SiN stripe at the top centre, and the stripe running along the normal to the cleaved surface.

Fits were performed for measurements on two different SiN stripes on InP. One SiN stripe had a nominal width of 20 $\mu$m (26JUL17B) and the other SiN stripe had a nominal width of 10 $\mu$m (26JUL17C). Similar results were obtained for both samples. Results are presented here for the nominally 20 $\mu$m wide SiN stripe.

### 3.1. Fits to the PL yield

The PL yield (i.e., the total luminescence = $L_h + L_v$ or = $L_{h'} + L_{v'}$) was analyzed to provide values needed in the least squares fitting procedure.

Complementary error functions as functions of vertical distance $v$,

$$\frac{A}{2}\,\mathrm{erfc}\left(\frac{v_e - v}{\sigma\sqrt{2}}\right), \tag{12}$$

were fit to the PL yields to determine best-fit estimates of the locations of the top edges of the samples, $v_e$, and the full-width half-maximum (FWHM) resolutions. For a Gaussian function with scale parameter (i.e., standard deviation) $\sigma$, the FWHM = $2.35482\,\sigma$. Table 1 lists the values found. The value of $A$ gives the best-fit value of the PL yield for the substrate away from the top edge of the sample.

**Table 1. Fit parameters for fits to the PL yield for the 20 $\mu$m wide SiN stripe sample.**

| $h$ | $A$ | $v_e$ $\mu$m | $\sigma$ $\mu$m | FWHM $\mu$m |
|---|---|---|---|---|
| 10 | 7233.4 | 6.53 | 1.29 | 3.04 |
| 20 | 7136.8 | 6.52 | 1.29 | 3.03 |
| 30 | 7119.8 | 6.53 | 1.30 | 3.05 |
| 40 | 7138.6 | 6.47 | 1.35 | 3.18 |
| 50 | 7127.0 | 6.50 | 1.35 | 3.17 |
| 60 | 7156.4 | 6.53 | 1.36 | 3.21 |
| 70 | 7159.2 | 6.53 | 1.36 | 3.20 |
| 80 | 7155.6 | 6.59 | 1.31 | 3.09 |
| 90 | 7111.3 | 6.63 | 1.31 | 3.09 |

Figure 3 shows the fit of an erfc to the PL yield for the sample with the 20 $\mu$m wide SiN stripe for $h = 50$, where $h$ is the horizontal distance. The top left edge of the sample occurs at the ordered pair $(h = 1, v_e)$, the top right edge occurs at $(h = 101, v_e)$, and the middle of the SiN stripe is roughly $(h = 50, v_e)$. For this file, the measurements were made on a grid with equal horizontal and vertical step distances, with $v_{step} = h_{step} = 0.5$ $\mu$m.

The PL yield, measured $DOP_{110}$, and measured $ROP_{110}$ for the 20 $\mu$m wide SiN stripe are displayed by Fig. 4. The data are low noise data, with rms values for the measured DOP and measured ROP data of 50 measurement units, or rms noise equivalents for measured DOP (or measured ROP) data of 0.05%. The noise levels were estimated from fits of FEM simulations to the data.

The left hand column of Fig. 4 shows the PL yield (top panel), the measured $DOP_{110}$ (middle panel), and the measured $ROP_{110}$ (bottom panel) for thresholding at $0.01 \times PL_{\max}$ where $PL_{\max}$ is the maximum value of the PL yield. The threshold of $0.01 \times PL_{\max}$ corresponds to roughly 5× the rms PL noise. Data that is below the threshold level is displayed in a magenta colour. The measured DOP and the measured ROP are dominated by noise for small values of the PL yield as

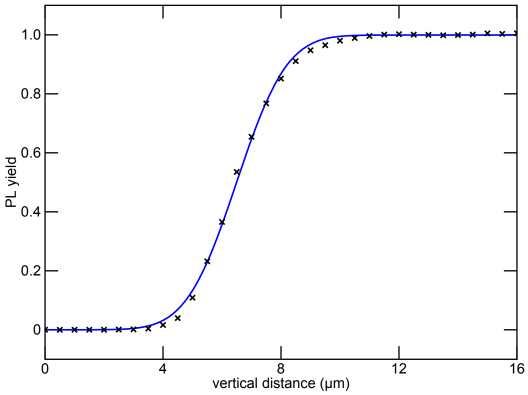

**Fig. 3.** Fit of a complementary error function to the PL data of the sample with the 20 $\mu$m wide SiN stripe as a function of the vertical distance $v$ from the top of the file and near the mid-point of the stripe, i.e., at $h = 50$.

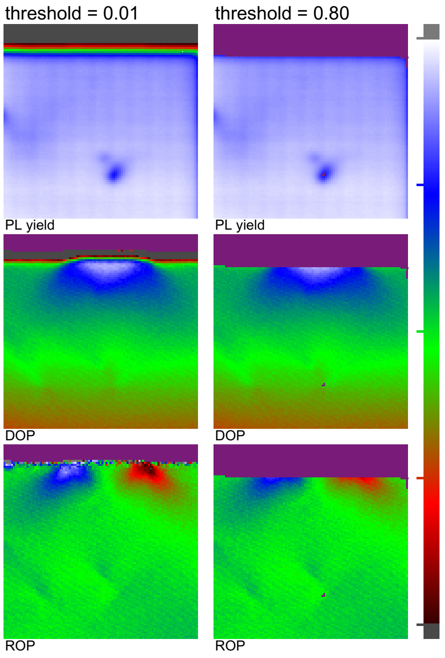

**Fig. 4.** From top to bottom, PL yield, measured $DOP_{110}$, and measured $ROP_{110}$ data. The PL threshold level was set to $0.01 \times PL_{\max}$ for the left column and to $0.80 \times PL_{\max}$ for the right column of three panels. The SiN stripe is approximately centred left-right in each panel and $\approx 6.5$ $\mu$m below the top boundary of each panel. Each panel displays data for the same area of $50$ $\mu$m $\times$ $50$ $\mu$m. See Sec. 3.2 for a description of the colour bar and the use of colour.

the measured DOP and ROP are the differences of the polarized PL yields along two orthogonal directions, as indicated by Eqs. (1) and (2).

The SiN stripe is approximately centred left-right and at the top of the InP substrate in the false colour maps. The top surface of the InP is, from Table 1, located at $v_e \approx 6.5$ $\mu$m below the top boundary of each panel. The SiN is centred above the blue 'blobs' of DOP shown in the middle panels and between the blue and red 'blobs' of ROP shown in the bottom panels. Each panel of Fig. 4 shows an area of 50 $\mu$m × 50 $\mu$m.

The right hand column displays the PL yield, the measured $DOP_{110}$, and the measured $ROP_{110}$ for thresholding at $0.80 \times PL_{\max}$. Thresholding at this value removes DOP and ROP data that are corrupted by noise and edge effects, as can be observed by comparing the left and right columns of the figure. Data sets created by thresholding at $0.80 \times PL_{\max}$ were used in the least squares fits of 3D FEM simulations to the measured DOP and ROP. Edge effects are features in the PL, DOP, and ROP that occur near the edge of the sample. These features might or might not be related to strain in the sample.

### *3.2. Colour Bar*

The three false-colour maps, of which Fig. 4 is an example, display two dimensional data using a mapping of colour to value. The colour bars of each figure display the mapping of value to colour and are composed of 241 rectangles of equal size (excluding the black and grey off-scale squares at the tops and bottoms of the colour bars) to represent 241 integers, with the colour-mapping running sequentially from smallest integer to largest integer from the bottom to the top of the colour bar.

The colour of the black square at the bottom of a colour bar is used to indicate values that are off-scale in the negative direction; the colour of the grey rectangle at the top of a colour bar is used to indicate values that are off-scale in the positive direction.

The dark-red colour that is just above the black square represents the smallest integer that can be uniquely displayed. The white colour just below the grey square is used to represent the largest integer that can be uniquely displayed. The three coloured tic marks indicate 25%, 50%, and 75% of the full scale of 241 integers. The height of a tic mark is equal to the height of any one of the 241 rectangles of the colour bar.

The data to be displayed by the false colour mapping is offset and multiplied by a display gain, and rounded to the nearest integer. The display gain is usually selected to use as many as possible of the 241 colours that are available.

The PL data is unipolar; the PL can not be negative. For PL data, zero is mapped to the black off-scale colour square at the bottom of the colour bar. The PL data is recorded in arbitrary units and thus the display gain is not important. The relative strengths of the PL yields for different areas on the sample are determined by the mapping shown in the colour bar.

The DOP and ROP are bipolar signals. These signals can be positive or negative. An offset is used to map zero to the midpoint of the colour bar (which is at the green tic mark) and a display gain is selected to use as many colours as possible. For all the false colour maps of the DOP, a display gain of 12 was chosen. This means that the just off-scale colours are equal to a DOP of $\pm 0.0243$ relative to the green tic mark.

For all false colour maps of the ROP, a display gain of 18 was chosen. The just off-scale colours for the ROP maps are equal to a ROP of $\pm 0.0162$ relative to the green tic mark.

For false colour maps of the residues, the display gains were multiplied by 5. Thus the just off-scale colours for the DOP and ROP residues are five times smaller than for the DOP and ROP.

The DOP and ROP are the differences of two nearly equal numbers divided by the sums of two nearly equal numbers; see Eqs. (1) and (2). If the PL yield is low, then the DOP and ROP are dominated by noise. For areas with PL below a user-selected threshold value, the values are mapped to a magenta (purple) colour.

Each panel in all the false-colour images displays data for the same 50 $\mu$m × 50 $\mu$m area of the sample. The false-colour maps are composed of colour-filled squares, with one square for each measurement at position $(h_i, v_i)$. The measured value at each $(h_i, v_i)$ is offset as appropriate, multiplied by the display gain, rounded to the nearest integer, and the corresponding square is filled with the colour as specified by the integer and as displayed by the colour bars.

## 4. Fits of FEM simulations to an InP chip with a nominal 20 $\mu$m wide SiN stripe

3D FEM simulations were performed on an InP substrate that was assumed to be 100 $\mu$m thick and using coordinate scaling [23] ($y_{scale} = 4$) for the thin SiN layer. The FEM simulations in the plane of the facet were output on a 0.25 $\mu$m grid, were convolved with a Gaussian function of 3.06 $\mu$m FWHM, which is the average FWHM to the left and right of the SiN stripe (see Table 1), shifted by $(-7, 25)$, and downsampled to match the experimental data.

Values for the thickness and material constants were assumed: the SiN true thickness was taken to be 0.5 $\mu$m, with $E_{\mathrm{SiN}} = 230$ GPa, and $\nu_{\mathrm{SiN}} = 0.33$. The values for $E_{\mathrm{SiN}}$ and $\nu_{\mathrm{SiN}}$ were obtained by fitting FEM simulations of different values to the data and taking the values that were near the minima of $\chi_T$ and that were consistent for both samples. The minima in $\chi_T$ as functions of $E_{\mathrm{SiN}}$ and $\nu_{\mathrm{SiN}}$ were found to be shallow and broad.

The elements $C_{ij}$ of the SiN stiffness matrix $[C]$ were taken to be

$$G_{\mathrm{SiN}} = \frac{E_{\mathrm{SiN}}}{2\,(1 + \nu_{\mathrm{SiN}})} \tag{13}$$

$$C_{11} = \frac{E_{\mathrm{SiN}} \times (1 - \nu_{\mathrm{SiN}})}{(1 + \nu_{\mathrm{SiN}}) \times (1 - 2\,\nu_{\mathrm{SiN}})} \tag{14}$$

$$C_{12} = \frac{E_{\mathrm{SiN}} \times \nu_{\mathrm{SiN}}}{(1 + \nu_{\mathrm{SiN}}) \times (1 - 2\,\nu_{\mathrm{SiN}})} \tag{15}$$

with $C_{22} = C_{33} = C_{11}$, $C_{13} = C_{23} = C_{12}$, $C_{66} = C_{44} = G_{\mathrm{SiN}}$.

In the crystal coordinate system, the three independent elements of the stiffness matrix for InP were taken to be $C_{11} = 102.2 \pm 0.9$ GPa, $C_{12} = 57.3 \pm 0.9$ GPa, $C_{44} = 44.2 \pm 2.2$ GPa [8,24]. The 3D FEM simulations were performed using the measurement coordinate system, for which the $h$ and $v$ directions lie in the plane of the facet and $v$ points along the '3' axis of the crystal coordinate system. This measurement coordinate system is obtained by rotation of the crystal coordinate system by 45 deg about the '3' or $z$ axis of the crystal coordinate system. The elements of the InP stiffness matrix in the measurement coordinate system were obtained by rotation of the stiffness tensor, are symmetric with respect to the matrix diagonal, and are given by $C_{11} = C_{22} = 123.95$ GPa, $C_{33} = 102.2$ GPa, $C_{44} = C_{55} = 44.2$ GPa, $C_{66} = 22.45$ GPa, $C_{12} = 35.55$ GPa, $C_{13} = 57.3$ GPa.

Simulations were performed for various widths of the stripe, from 18 $\mu$m to 25 $\mu$m in 1 $\mu$m increments, plus 21.5 $\mu$m to 22.5 $\mu$m in 0.25 $\mu$m increments. Minimum values of $\chi_T$ were found for a width of 22.25 $\mu$m.

Biaxial strain (as an initial condition for the FEM simulations) in a 22.25 $\mu$m wide stripe SiN appear to fit the data well and accounts for the majority of the measured $DOP_{110}$ and $ROP_{110}$ patterns. It is interesting to note that biaxial strain in the SiN was preferred over biaxial stress in the SiN. The value for $\chi_T$ for biaxial strain was one 95 % confidence interval lower than for the $\chi_T$ that was obtained with biaxial stress in the SiN.

The best fit, i.e, a minimum value for $\chi_T$, was found to occur for a registration of $(-7, 23)$. From the PL fits, $v_e$, where $v_e$ is the top edge of the sample, is expected at 26 quarter $\mu$m steps from the top of the file, and not 23. Results reported here are for registrations of $(-7, 25)$ quarter $\mu$m steps. The registration is uncertain by at least one quarter $\mu$m step to account for different counting methods used for the FEM simulation and data. It was decided to use the registration that was midway between the $v_e$ that gave the minimum for $\chi_T$ and $v_e$ as determined by fits to the PL. The results show a weak dependence on the value of $v_e$.

Table 2 lists the scaled relative changes in $\chi_T$, $(\chi_T - \min(\chi_T))\,/CI_{0.95}$, for various values for registrations of $(h_i, v_e)$. The minimum value of $\chi_T$ occurs at $(-7, 23)$ and equals $0.93233 \pm 0.011$, where $\pm 0.011$ is the estimated 95% confidence interval, $CI_{0.95}$. The table shows that the minimum at $(-7, 23)$ is well defined. However, the difference in $\chi_T$ between $(-7, 23)$ and $(-7, 25)$ is statistically insignificant, i.e., less than one 95% confidence interval.

**Table 2. Scaled relative changes in $\chi_T$ for various registrations $(h_i, v_e)$ around the minimum value of $\chi_T$. The changes are scaled by the 95% confidence interval $CI_{0.95}$.**

|  | $4\,v_e$ |  |  |  |  |
|---|---|---|---|---|---|
|  | 22 | 23 | 24 | 25 | 26 |
| $h_i = -8$ | 0.7 | 0.6 | 0.6 | 1.1 | 2.0 |
| $h_i = -7$ | 0.2 | 0.0 | 0.1 | 0.5 | 1.4 |
| $h_i = -6$ | 0.7 | 0.5 | 0.6 | 1.0 | 2.0 |

### 4.1. Exclusions

The rules for exclusions of data from the fit were quite simple. Any data point with a PL yield less than 80 % of the maximum PL yield (the PL maximum occurs at the lower left and has a value of $PL_{max} = 7757$) was excluded from the fit. This 80 % rule also removed three data points in the interior of DOP maps. This removal is convenient as these three removed points provide a reference point on the maps of PL yield, DOP, and ROP.

### 4.2. Results of fits

Figure 5 shows the data, fits, and residues. The residue is defined as the data minus the fit and is displayed with a gain of 5× more than for the data and fits. The fits of FEM simulations to the data appear to be good. Patterns from defects (likely dislocations [11,12,25]) are evident in the maps of the residues, and it is difficult to determine if some of the coloured lobes under the stripe are from defects or from the FEM simulations missing some aspects of the true strain field.

Measurements for which the PL yield is below the threshold values are displayed in magenta for maps of the PL, DOP and ROP. Areas of magenta thus indicate areas of low PL, such as areas where the PL beam is not fully on the sample. Figure 3 and the $v_e$ column of Table 1 shows that at least the top 16 rows should be displayed in magenta, as the PL yields for these rows are likely below $0.80 \times PL_{max} \approx 6200$. The panel at the top of Fig. 5 display the measured $DOP_{110}$ and $ROP_{110}$. The top parts of these panels are displayed in magenta since the PL yield is weak as the pump beam is not on or only partially on the sample for these parts.

Thresholding of the PL yield at 80 % for the bottom half of the maps left a group of 3 pixels (mid, bottom quarter) that were below the threshold. These pixels are evident in all the panels of Fig. 5. The maps of the residues show that strain fields associated with a defect appear to be centred on this region of reduced PL yield. The residues, which are shown in the bottom panels of Fig. 5, show DOP and ROP patterns over extended areas that are centred on this area of slightly reduced PL yield.

Figure 6 shows development of the residue, defined as 5× (data subtract the best fit FEM simulation), for 1, 2, 3, and 4 basis functions. The magnitudes of the changes in $\chi_T$ for addition of a basis function can be determined from Table 3. Note that the entries in Table 3 are ordered by the influences that gave the largest changes in $\chi_T$.

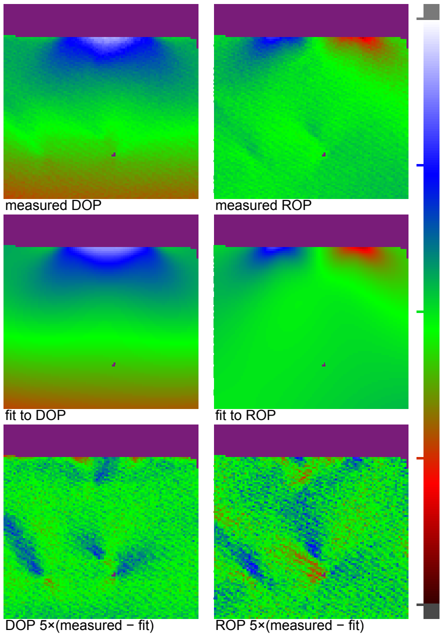

**Fig. 5.** From top to bottom: data; best fit function; and residue. The left-hand column displays data for fits to the DOP and the right hand column displays data for fits to the ROP. Each panel displays data for the same area of 50 $\mu$m × 50 $\mu$m. See Sec. 3.2 for a description of the colour bar and the use of colour.

**Table 3. $\chi$ values for fits of measured DOP and ROP data to FEM simulations for a 22.25 $\mu$m wide SiN stripe on InP at offsets of (midpoint, 4 $v_e$) = (−7, 25).**

| elements | influence | $\chi_T$ | $\chi_{DOP}$ | $\chi_{ROP}$ | $\delta\chi_T/CI_{0.95}$ |
|---|---|---|---|---|---|
| 0+1 | 1: biaxial strain in SiN | 1.0107 | 1.0916 | 0.9228 | −875 |
| 0+1+2 | 2: uniaxial $\hat{\boldsymbol{n}}$ polishing stress | 0.9658 | 1.0182 | 0.9102 | −4.2 |
| 0+1+2+3 | 3: uniaxial $h$ SiN stress | 0.9540 | 1.0004 | 0.9052 | −1.1 |
| 0+1+2+3+4 | 4: biaxial etch stress | 0.9368 | 0.9695 | 0.9030 | −1.6 |
| 0 | 0: background | 10.33 | 14.2 | 3.45 | |

In Table 3, $\delta\chi_T$ is the change in $\chi_T$ for addition of a basis function to the fit and $CI_{0.95}$ is the 95 % confidence interval for a single measurement of $\chi_T$. The 95 % confidence interval provides a metric for estimation if a change in $\chi_T$ is statistically significant. Since $\chi_T$ is a random variable, a random-fluctuation-induced difference between two independent measures of $\chi_T$ should be greater than $\sqrt{2}\,CI_{0.95}$ only 5 % of the time. Statistically, the 95% uncertainty in reduced chi, $CI_{0.95}$, is estimated for the fits reported here as $CI_{0.95} = \pm 0.01065 = \pm\sqrt{1.92/\nu}$ where $\nu = 16\,936$ is the number of degrees of freedom [14, Sec. 2B].

Thus from Table 3, it appears that addition of the first two basis functions and perhaps the last basis function yield a statistically significant reduction in $\chi_T$. This conclusion is consistent with a visual comparison of the columns in Fig. 5.

The value of $\delta\chi_T/CI_{0.95} = -4.2$ in Table 3 was calculated as $(0.9658 - 1.0107)/0.01065$. The value of −875 was calculated as $(1.0107 - 10.22)/0.01065$ and gives a measure of the magnitudes of the DOP and ROP signals. The background $\chi$ values were calculated as the rms of the difference between the data and the background, which was calculated as the best fit with all influences $(0 + 1 + 2 + 3 + 4)$ minus the calculated influence of $(1 + 2 + 3 + 4)$. The subtraction

OPTICS CONTINUUM

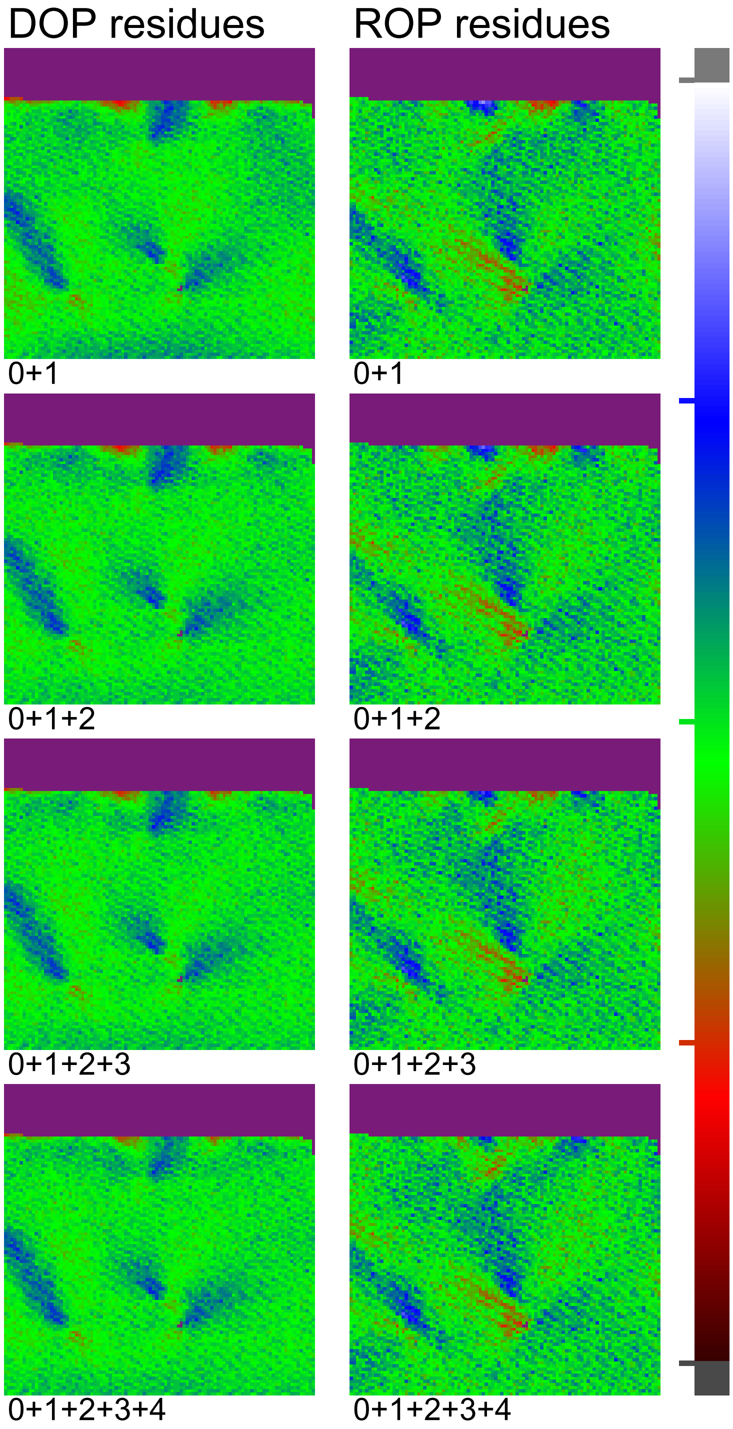

**Fig. 6.** Residues for, from top to bottom, fits using 0 + 1, 0 + 1 + 2, 0 + 1 + 2 + 3, 0 + 1 + 2 + 3 + 4 basis functions. The left hand column displays data for fits to the DOP and the right hand column displays data for fits to the ROP. Each panel displays data for the same area of 50 $\mu$m × 50 $\mu$m. See Sec. 3.2 for a description of the colour bar and the use of colour.

to produce the difference removes the estimate of the contribution owing to the SiN stripe and thus provides a reference 'plane' for calculation of the rms value of the DOP and ROP lobes under the SiN stripe. The value of −875 for the reduction of $\delta\chi_T/CI_{0.95}$ by the biaxial strain initial condition in the SiN indicates that the biaxial strain basis function accounts for the vast majority of the DOP and ROP signals created by the SiN stripe.

3D FEM simulations were performed for 24 different influences as initial conditions. These influences included biaxial and two uniaxial stresses and strains in the SiN, biaxial and uniaxial polishing stresses and strain on the bottom of the InP, interface stress between the SiN and InP, and etching stresses and strains on the exposed InP beside the SiN. The least squares fitting looped over all influences and backgrounds and accepted the influence that created the smallest value of $\chi_T$. This influence was accepted as the '0+1' element and the procedure was repeated to find the four elements that gave a minimum value for $\chi_T$. It is interesting to note that biaxial strain in the SiN was slightly preferred ($\chi_T = 1.0107$) over biaxial stress in the SiN ($\chi_T = 1.0214 = 1.0107 + 1.004 \times CI_{0.95}$) as the primary influence.

The choices of influences accepted for Table 3 are not necessarily statistically unique. For the first row, there were two choices: biaxial strain or biaxial stress in the SiN. Fits with an initial condition of biaxial strain in the SiN yielded the smallest $\chi_T$ of all the 24 basis functions that were considered. Fits with biaxial stress in the SiN yielded a $\chi_T$ that was $1.004 \times CI_{0.95}$ greater than the $\chi_T$ found with biaxial stress. Any other basis functions gave a $\chi_T$ that was at least greater by $42 \times CI_{0.95}$ than the $\chi_T$ found with biaxial strain.

For the second row of Table 3 there were 12 choices that gave $\delta\chi_T < CI_{0.95}$. Most of the choices were similar, in that the choice of influence was an uniaxial influence, suggesting some asymmetry between the simulation and the data. The uniaxial polishing strain was chosen because it produced the largest $\delta\chi_T$, even though this change was not statistically different from other influences.

For the third row of Table 3, there were eight choices. The top choices, as measured by the largest $\delta\chi_T$, were for uniaxial stress or strain in the SiN. Again, this suggests some asymmetry between the simulation and the data. This asymmetry might arise from the different shapes assumed for the FEM simulation and the shape of the sample.

For the last row of Table 3, there were six choices that gave $\delta\chi_T < CI_{0.95}$. The first five of these six choices, as ranked by magnitude of $\delta\chi_T$, were for strains or stresses on the top surface of the InP that was outside the SiN stripe. This suggests a weak contribution from the InP surface to the left and right of the SiN stripe.

The top two panels of Fig. 6 show the residues when only one basis function (biaxial strain in the SiN) plus the background terms are used. A comparison of Figs. 5 and 6 shows that the majority of the DOP and ROP patterns are accounted for by the biaxial strain plus the background terms. Note that the residues are displayed with a display gain of 5× greater than the display gain used to display data for fits.

The second row from the top shows the residues when uniaxial $\hat{\boldsymbol{n}}$ polishing stress is added to the fit, where $\hat{\boldsymbol{n}}$ is in the direction of a normal to the facet. The addition of the uniaxial polishing stress seems to provide a (barely) visually noticeable change in the DOP residue. This change is noticeable at the top of the sample, where the red to the left and right of the SiN stripe and adjacent to the magenta is visible in the top DOP panel but not so much in the second-to-top DOP panel.

The third row of panels from the top shows the residues for addition of an uniaxial $h$ SiN strain. The addition of this basis function does not appear to produce a visually noticeable change in the residues.

The addition of a biaxial strain on the top surface of the InP and to the left and right of the SiN stripe appears to reduce visually the residue, as can be observed by comparing the bottom row of panels to the row of panels above the bottom row. The red and blue areas that are under the SiN and at the top of the InP, close to the magenta coloured area, appear to be reduced in size and magnitude.

If one uses the ability to perceive visually differences in the pattern of residues as the criterion for a significant change in the quality of fit, it appears that changes of reduced chi of $\approx 0.02$ are significant. Since reduced chi is calculated over a large area, it is likely that a pattern over a small area, as in the case for the ROP residue, would be visible over random fluctuations even if it caused a change in reduced chi that is smaller than the overall statistical uncertainty.

A value of $R_a = 0.83$ was used to produce the false colour images presented here. $R_a$ gives the ratio of the ROP to the DOP fit coefficients. A value of unity for $R_a$ is expected if the predictions of [13] are correct, i.e., if Eqs. (5) and (6) are correct and if the ratio of $d/b = 2.5$ is correct [15, Table VI, pg 5829].

A ratio of $0.967 = 1.415/1.463$ was found for fits of FEM simulations to loaded v-grooves in InP [14, Table 3] assuming $d/b = 2.5$. In Ref. [14] the factor of 1.463 was not included in the expression for $ROP_{110}$. The value of the ratio as determined from this work is 0.83, which is significantly less than the value of 0.967 which was found for fits to a loaded v-groove.

The reason for the discrepancy between the v-groove results and the results obtained here for an SiN stripe is not known. It is possible that fits to the SiN stripe are perturbed by defects in the substrate. Figure 6 shows patterns which look like defects in the substrate (likely dislocations [11,12,25]). It does not seem possible to determine if the blue lobes and the red lobes under the stripe are from defects or are residues from the use of inadequate basis functions. Nevertheless, $R_a = 0.83$ plus the results from the v-groove fits suggest that the isotropic model is not an appropriate description of the $DOP_{110}$ or $ROP_{110}$ strain dependence. For an isotropic model, one would expect to find $R_a = 1.463$ rather than unity. Fits of an isotropic model, Eqs. (3) and (4), give $R_a = 1.25$.

It is not possible to distinguish between Eqs. (3) and (5) based on fits to measured DOP data, since $DOP$ and $DOP_{110}$ are essentially degenerate for biaxial strain in an SiN stripe. This point is discussed in the Appendix.

## 5. Conclusion

The measured data are low noise and fits of 3D FEM simulations of a 22.25 $\mu$m wide SiN stripe on InP seem to fit the measured data of a sample with a nominally 20 $\mu$m wide SiN stripe remarkably well. Least squares fits of simulations to measured DOP and ROP show that the vast majorities of the DOP and ROP patterns (>99% if one compares $\delta\chi_T$) are explained by an initial condition for the FEM simulations of biaxial strain in the SiN stripe.

Assuming a calibration constant of $|K_e| = 3\,b/(4\,k_B\,T) = 58 \mp 0.6$ with $b = 2$, $T = 296 \pm 3$, and a 95% uncertainty in the least squares fit coefficient of 0.004, this gives a biaxial strain of $(-3.3 \pm 0.05) \times 10^{-4}$ in the SiN. Assuming $E = 230$ GPa and $\nu = 0.33$, this gives a stress of $(-3.3 \pm 0.05) \times 10^{-4}\,E/(1-\nu) = -112 \pm 2$ MPa in the SiN. The shear deformation potentials $b$ and $d$ are experimentally determined numbers. Any uncertainty assigned to $b$ or $d$ means additional uncertainty in the estimated stresses and strains.

Fits of FEM simulations to the DOP and ROP data provide evidence, in addition to fits of FEM simulations to loaded v-grooves [14], to the predictions of [13] for the dependence of DOP and ROP on strain. See Eqs. (3) – (6) of this note for examples of the predictions for the dependence of DOP and ROP on strain for $\{110\}$ InP facets, assuming $d = 2.5\,b$. Results, based on the ratio $R_a$ of the magnitudes of the fit coefficients for the DOP and ROP components, lie between the value expected for the isotropic model of Eqs. (3) – (4) and the value expected from Eqs. (5) – (6). The reason for the discrepancy is unknown, but might lie in the fits being tainted by DOP and ROP patterns from defects existing in the InP substrate. These defects are apparent (c.f. Figures 5 and 6) in the residues of fits to the measured data.

As shown in the Appendix, the horizontal and vertical strain fields in the substrate under (an initial condition of) biaxially strained SiN stripe are similar. This makes it extremely difficult if not impossible to estimate the correct dependence of DOP on strain from only measurements of the degree of polarization (DOP) of luminescence from a cleaved facet of the substrate.

## 6. Appendix

For $d = \xi\, b$, where $b$ and $d$ are the shear deformation potentials [15, II.A.3 and Table VI], expressions for $DOP_{110}$ and $ROP_{110}$ are

$$DOP_{110} = \frac{3\,b}{4\,k_B\,T}\,[0.3926\,(\xi + 0.8495)\,e_1 + 0.1410\,(\xi - 8.1646)\,e_3] \tag{16}$$

and

$$ROP_{110} = \frac{-3\,b}{4\,k_B\,T}\,0.5851\,\xi\,(2\,e_5). \tag{17}$$

Owing to dependence of the proportions of $e_1$ and $e_3$ on $\xi$ in Eq. (16), one might hope to be able to estimate the value of $\xi$ for fits to the low-noise data presented in this paper. However, as can be observed from the 3D FEM simulations shown in Fig. 7, $e_3$ is approximately proportional to $-e_1$ and $DOP$ and $DOP_{110}$ are similar, as shown in Fig. 8.

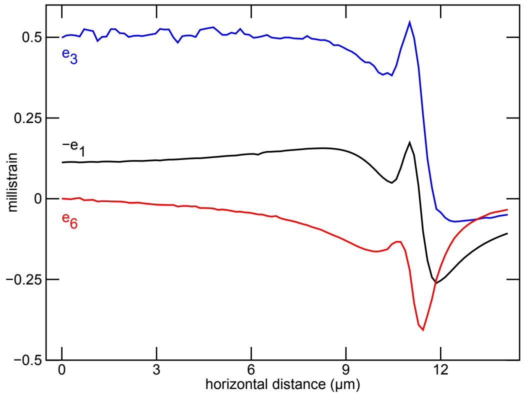

**Fig. 7.** Strains, 0.5 $\mu$m below the SiN, in the plane of the facet.

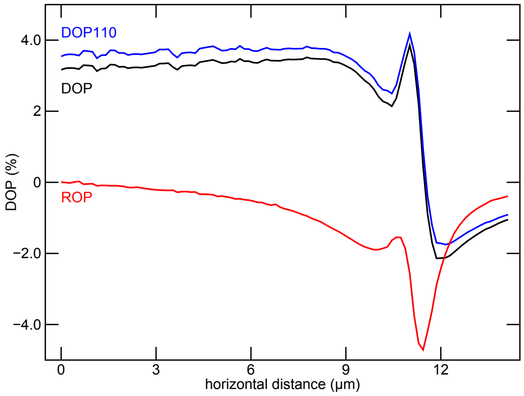

**Fig. 8.** $DOP_{110}$, $DOP$, and $ROP$, 0.5 $\mu$m below the SiN, in the plane of the facet.

The simulations for Figs. 7 and 8 are for a 22.25 $\mu$m wide SiN stripe on InP with an initial condition of biaxial strain in the '1' and '2' directions for the SiN stripe. Only the right-hand half of the strains and DOPs are shown in the figures; the $x = 0$ plane is a mirror plane. The curves for the figures are for the quantities evaluated at the facet and for a line that is parallel to the top surface of the InP and that is 0.5 $\mu$m below the SiN interface.

The curve labelled DOP110 was obtained for $\xi = 2.5$ whereas the curve labelled DOP is for $DOP = -|K_e|(e_1 - e_3)$, Eq. (3), which can be obtained from an expression for $DOP_{110}$ by assuming that the InP was isotropic [13, Sec. 4.1]. For isotropic material, $\xi = \sqrt{3} = 1.732$, $\gamma_3 = \gamma_2$, where $\gamma_3$ and $\gamma_2$ are Luttinger parameters which describe the valence band, and there are only two independent elastic constants. An expression for $DOP_{110}$ with no excess $e_1$ as compared to $e_3$ is also obtained for $d = 1.532\,b$ without assumptions on the Luttinger parameters or the elastic constants: $DOP_{110} = -0.935\,K_e\,(e_1 - e_3)$ for $\xi = 1.532$ [14, pg 4505, RHS].

From a comparison of the $DOP_{110}$ and $DOP$ curves of Fig. 8 and from the preceding discussion, it should be quite clear that it would be virtually impossible to provide an accurate estimate of the value of $\xi = d/b$ from fits of FEM simulations to the measured DOP of luminescence from under a biaxially-strained stripe of SiN.

The curves for $DOP_{110}$ and $DOP$ are obtained for greatly different values of $\xi$ yet are virtually identical (except for a scale factor). For the SiN/InP samples discussed here, the strains are unknown. Thus any least squares fit will adjust the values of the strains to match the measured data. To further complicate the determination of $\xi$ from the data, the values $b$ and $d$ are experimentally determined quantities with uncertainties ($b = -2.0^{+1.0}_{-0.0}$ eV and $d = -5.0^{+0.8}_{-0.0}$ eV [15, Table VI]) and the experimentally determined $DOP_{110}$ calibration constant $K_e$ for InP has an estimated uncertainty of ±12% [16, pp 101–103].

$ROP$ and $ROP_{110}$ are both proportional to the shear strain (c.f. Eqs. (4) and (6)), and thus there is no distinguishing feature that would indicate the choice of the ratio of $\xi$.

As a minimum, one should be able to distinguish between the isotropic model, which yields expressions for $DOP$ and $ROP$, and the model presented in [13], which yields expressions for $DOP_{110}$ and $ROP_{110}$, by forming the ratio of the fit coefficients. The correct model should yield a ratio $R_a = 1$.

For the $DOP_{110}$ model with $\xi = 2.5$, the ratio of the fit coefficients was found to be $R_a = 0.83$. For the $DOP$ model, the ratio of the fit coefficients was found to be $R_a = 1.25$. This result is not consistent with results found from fits to v-groove data [14], from which the ratio of the fit coefficients was found to be $1.41/1.463 = 0.96$ for the $DOP_{110}$ model with $\xi = 2.5$.

Since $0.83 \times 1.463 = 1.21$, the fits to the data seems to suggest that $1.6 < \xi < 2.5$. The result is also not consistent with the recommended values for $b$ and $d$ [15, Table VI].

The inconsistent result might be the result of contamination of the fit by pre-existing defects in the InP substrate. These pre-existing defects are visible in Figs. 5 and 6. With no defects and a good fit, one would expect to see a false colour map of the residues as a uniform green, where green is mapped to zero.

**Disclosures.** The authors declare no conflicts of interest.

**Data availability.** Data underlying the results presented in this paper are not publicly available at this time but may be obtained from the authors upon reasonable request.

## References

1. M. G. Daly, D. M. Bruce, P. E. Jessop, D. T. Cassidy, and D. Yevick, "Metallization stress in weakly guiding InP/InGaAsP waveguides," Semicond. Sci. Technol. **9**(7), 1387–1390 (1994).
2. G. B. Morrison, D. T. Cassidy, J. E. Johnson, M. Sipics, H. Wang, and R. Wolf, "Bonding-induced strain effects in InP DFB components soldered p-side-up on AlN substrates," IEEE J. Quantum Electron. **45**(8), 937–944 (2009).
3. D. Lisak, D. T. Cassidy, and A. H. Moore, "Bonding stress and reliability of high-power GaAs-based lasers," IEEE Trans. Comp. Packag. Technol. **24**(1), 92–98 (2001).

4. S. K. K. Lam and D. T. Cassidy, “Multi-Component Model for Semiconductor Laser Degradation,” in *Advanced Laser Diode Reliabilty*, M. Vanzi, L. Béchou, M. Fukuda, and G. Mura, eds. (ISTE Press Ltd, London, UK, 2020), pp. 51–75.
5. D. T. Cassidy and C. S. Adams, “Polarization of the output of InGaAsP semiconductor diode lasers,” IEEE J. Quantum Electron. **25**(6), 1156–1160 (1989).
6. P. D. Colbourne and D. T. Cassidy, “Bonding stress measurements from the degree of polarization of facet emission of AlGaAs superluminescent diodes,” IEEE J. Quantum Electron. **27**(4), 914–920 (1991).
7. P. D. Colbourne and D. T. Cassidy, “Imaging of stresses in GaAs diode lasers using polarization resolved photoluminescence,” IEEE J. Quantum Electron. **29**(1), 62–68 (1993).
8. D. T. Cassidy, S. K. K. Lam, B. Lakshmi, and D. M. Bruce, “Strain mapping by measurement of the degree of photoluminescence,” Appl. Opt. **43**(9), 1811–1818 (2004).
9. M. Born and E. Wolf, *Principles of Optics* (Cambridge University Press, 1993), 6 (corrected) Edition ed.
10. P. D. Colbourne, “Measurement of Stress in III-V Semiconductors using the Degree of Polarization of Luminescence,” Ph.D. thesis, McMaster University, http://hdl.handle.net/11375/6786, Hamilton, ON, Canada (1992).
11. P. D. Colbourne and D. T. Cassidy, “Observation of dislocation stresses in InP using polarization-resolved photoluminescence,” Appl. Phys. Lett. **61**(10), 1174–1176 (1992).
12. P. D. Colbourne and D. T. Cassidy, “Dislocation detection using polarization-resolved photoluminescence,” Can. J. Phys. **70**(10-11), 803–812 (1992).
13. D. T. Cassidy and J.-P. Landesman, “Degree of polarization of luminescence from GaAs and InP as a function of strain: a theoretical investigation,” Appl. Opt. **59**(18), 5506–5520 (2020).
14. D. T. Cassidy and S. K. K. Lam, “Degree of polarization of luminescence from facets of InP as a function of strain: some experimental evidence,” Appl. Opt. **60**(16), 4502–4510 (2021).
15. I. Vurgaftman, J. R. Meyer, and L. R. Ram-Mohan, “Band parameters for III-V compound semiconductors and their alloys,” J. Appl. Phys. **89**(11), 5815–5875 (2001).
16. J.-P. Landesman, D. T. Cassidy, J. W. Tomm, and M. L. Biermann, “Strain measurement,” in *Quantum-Well Laser Array Packaging: Nanoscale Packaging Techniques*, J. W. Tomm and J. Jiménez, eds. (McGraw-Hill Companies, New York, 2007).
17. T. B. Bahder, “Analytic disperson relations near the Γ point in strained zinc-blende crystals,” Phys. Rev. B **45**(4), 1629–1637 (1992).
18. T. B. Bahder, “Eight-band $\mathbf{k} \cdot \mathbf{p}$ model of strained zinc-blende crystals,” Phys. Rev. B **41**(17), 11992–12001 (1990).
19. T. B. Bahder, “Erratum: Eight-band $\mathbf{k} \cdot \mathbf{p}$ model of strained zinc-blende crystals [Phys. Rev. B 41, 11992 (1990)],” Phys. Rev. B **46**(15), 9913 (1992).
20. G. Lasher and B. Stern, “Spontaneous and stimulated emission in semiconductors,” Phys. Rev. **133**(2A), A553–A563 (1964).
21. P. R. Bevington and D. K. Robinson, *Data Reduction and Error Analysis for the Physical Sciences*, 2 Edition (McGraw Hill, Inc., New York, 1992).
22. S. J. Lascos and D. T. Cassidy, “Optical phase and intensity modulation from a rotating optical flat: effect on noise in degree of polarization measurements,” Appl. Opt. **48**(9), 1697–1704 (2009).
23. https://www.pdesolutions.com/help/coordinatescaling.html, *Technical Notes* (2022).
24. A. D. Prins and D. J. Dunstan, “Compliance of InP,” in *Properties of Indium Phosphide EMIS Datareviews Series 6*, (Inspec, London, 1991).
25. D. T. Cassidy, “Spatially resolved and polarization resolved photoluminescence for study of strain and dislocations in III-V materials,” Mater. Sci. Eng. B **91-92**, 2–9 (2002).